

## REPORT DOCUMENTATION PAGE

Form Approved OMB NO. 0704-0188

The public reporting burden for this collection of information is estimated to average 1 hour per response, including the time for reviewing instructions, searching existing data sources, gathering and maintaining the data needed, and completing and reviewing the collection of information. Send comments regarding this burden estimate or any other aspect of this collection of information, including suggestions for reducing this burden, to Washington Headquarters Services, Directorate for Information Operations and Reports, 1215 Jefferson Davis Highway, Suite 1204, Arlington VA, 22202-4302. Respondents should be aware that notwithstanding any other provision of law, no person shall be subject to any penalty for failing to comply with a collection of information if it does not display a currently valid OMB control number.  
PLEASE DO NOT RETURN YOUR FORM TO THE ABOVE ADDRESS.

1. REPORT DATE (DD-MM-YYYY) 22-12-2014	2. REPORT TYPE Final Report	3. DATES COVERED (From - To) 1-Sep-2011 - 31-Aug-2014		
4. TITLE AND SUBTITLE Thermal Properties of Whispering Gallery Mode Resonators		5a. CONTRACT NUMBER W911NF-11-1-0423		
		5b. GRANT NUMBER		
		5c. PROGRAM ELEMENT NUMBER 611102		
6. AUTHORS Lan Yang		5d. PROJECT NUMBER		
		5e. TASK NUMBER		
		5f. WORK UNIT NUMBER		
7. PERFORMING ORGANIZATION NAMES AND ADDRESSES Washington University Campus Box 1054 One Brookings Drive St. Louis, MO 63130 -4862		8. PERFORMING ORGANIZATION REPORT NUMBER		
9. SPONSORING/MONITORING AGENCY NAME(S) AND ADDRESS (ES) U.S. Army Research Office P.O. Box 12211 Research Triangle Park, NC 27709-2211		10. SPONSOR/MONITOR'S ACRONYM(S) ARO		
		11. SPONSOR/MONITOR'S REPORT NUMBER(S) 60386-EL.4		
12. DISTRIBUTION AVAILABILITY STATEMENT Approved for Public Release; Distribution Unlimited				
13. SUPPLEMENTARY NOTES The views, opinions and/or findings contained in this report are those of the author(s) and should not be construed as an official Department of the Army position, policy or decision, unless so designated by other documentation.				
14. ABSTRACT In this project, we studied the thermal properties of ultra-high-quality whispering-gallery-mode microtoroid resonators. More specifically, we measured the thermal relaxation time of the resonator to estimate the response time of the resonator based infrared (IR) detector. We found that, depending on the size of the silicon pillar, thermal relaxation time of the resonators can vary from a few hundred micro-seconds to a few milli-seconds. We also characterized the performance of a microtoroid IR detector by measuring its response to an IR radiation source. By varying the illumination conditions and modulation frequency of the IR source, we characterized the IR sensitivity.				
15. SUBJECT TERMS whispering-gallery-mode resonators, infrared sensing, thermal analysis				
16. SECURITY CLASSIFICATION OF: a. REPORT UU		17. LIMITATION OF ABSTRACT UU	15. NUMBER OF PAGES	19a. NAME OF RESPONSIBLE PERSON Lan Yang
b. ABSTRACT UU		c. THIS PAGE UU		19b. TELEPHONE NUMBER 314-935-9543



## Report Title

Thermal Properties of Whispering Gallery Mode Resonators

### ABSTRACT

In this project, we studied the thermal properties of ultra-high-quality whispering-gallery-mode microtoroid resonators. More specifically, we measured the thermal relaxation time of the resonator to estimate the response time of the resonator based infrared (IR) detector. We found that, depending on the size of the silicon pillar, thermal relaxation time of the resonators can vary from a few hundred micro-seconds to a few milli-seconds. We also characterized the performance of a microtoroid IR detector by measuring its response to an IR radiation source. By varying the illumination conditions and modulation frequency of the IR source, we characterized the IR sensitivity and the response bandwidth of the silica microtoroids. Our results show that high-quality WGM microtoroid resonators have the potential to compete with the state-of-the-art microbolometer detectors.

---

**Enter List of papers submitted or published that acknowledge ARO support from the start of the project to the date of this printing. List the papers, including journal references, in the following categories:**

**(a) Papers published in peer-reviewed journals (N/A for none)**

Received      Paper

11/05/2012 1.00 Jiangang Zhu, S?ahin Kaya O?zdemir, Lina He, Lan Yang. Optothermal spectroscopy of whispering gallery microresonators,  
Applied Physics Letters, ( 2011): 0. doi: 10.1063/1.3656716

11/30/2014 2.00 Sahin Kaya Ozdemir, Faraz Monifi, Junsoo Park, Tandeep Chadha, Steven He Huang, Pratim Biswas, Lan Yang. Titanium Dioxide Whispering Gallery Microcavities,  
Advanced Optical Materials, (08 2014): 711. doi: 10.1002/adom.201400107

11/30/2014 3.00 Jiangang Zhu, Sahin Kaya Ozdemir, Lan Yang. Infrared light detection using a whispering-gallery-mode optical microcavity,  
Applied Physics Letters, (04 2014): 171114. doi: 10.1063/1.4874652

**TOTAL:**      **3**

**Number of Papers published in peer-reviewed journals:**

---

**(b) Papers published in non-peer-reviewed journals (N/A for none)**

Received      Paper

**TOTAL:**

**Number of Papers published in non peer-reviewed journals:**

---

**(c) Presentations**

**Number of Presentations:** 0.00

---

**Non Peer-Reviewed Conference Proceeding publications (other than abstracts):**

Received      Paper

**TOTAL:**

**Number of Non Peer-Reviewed Conference Proceeding publications (other than abstracts):**

---

**Peer-Reviewed Conference Proceeding publications (other than abstracts):**

Received      Paper

**TOTAL:**

**Number of Peer-Reviewed Conference Proceeding publications (other than abstracts):**

---

**(d) Manuscripts**

Received      Paper

**TOTAL:**

**Number of Manuscripts:**

---

**Books**

Received      Book

**TOTAL:**

Received      Book Chapter

**TOTAL:**

**Patents Submitted**

---

**Patents Awarded**

---

**Awards**

---

**Graduate Students**

---

<u>NAME</u>	<u>PERCENT SUPPORTED</u>	Discipline
Faraz Monifi	0.19	
Guangming Zhao	0.03	
Jiangang Zhu	0.08	
<b>FTE Equivalent:</b>	<b>0.30</b>	
<b>Total Number:</b>	<b>3</b>	

### **Names of Post Doctorates**

<u>NAME</u>	<u>PERCENT SUPPORTED</u>
Sahin Kaya Ozdemir	0.17
Jiangang Zhu	0.42
<b>FTE Equivalent:</b>	<b>0.59</b>
<b>Total Number:</b>	<b>2</b>

### **Names of Faculty Supported**

<u>NAME</u>	<u>PERCENT SUPPORTED</u>	National Academy Member
Lan Yang	0.10	
Daniel Leon Rode	0.05	
<b>FTE Equivalent:</b>	<b>0.15</b>	
<b>Total Number:</b>	<b>2</b>	

### **Names of Under Graduate students supported**

<u>NAME</u>	<u>PERCENT SUPPORTED</u>	Discipline
Arunita Kar	0.00	Electrical and Systems Engineering
<b>FTE Equivalent:</b>	<b>0.00</b>	
<b>Total Number:</b>	<b>1</b>	

### **Student Metrics**

This section only applies to graduating undergraduates supported by this agreement in this reporting period

The number of undergraduates funded by this agreement who graduated during this period: ..... 1.00

The number of undergraduates funded by this agreement who graduated during this period with a degree in science, mathematics, engineering, or technology fields:..... 1.00

The number of undergraduates funded by your agreement who graduated during this period and will continue to pursue a graduate or Ph.D. degree in science, mathematics, engineering, or technology fields:..... 1.00

Number of graduating undergraduates who achieved a 3.5 GPA to 4.0 (4.0 max scale):..... 1.00

Number of graduating undergraduates funded by a DoD funded Center of Excellence grant for Education, Research and Engineering:..... 0.00

The number of undergraduates funded by your agreement who graduated during this period and intend to work for the Department of Defense ..... 0.00

The number of undergraduates funded by your agreement who graduated during this period and will receive scholarships or fellowships for further studies in science, mathematics, engineering or technology fields: ..... 0.00

### **Names of Personnel receiving masters degrees**

<u>NAME</u>
<b>Total Number:</b>

### **Names of personnel receiving PHDs**

<u>NAME</u>
Faraz Monifi
<b>Total Number:</b>

---

**Names of other research staff**

<u>NAME</u>	<u>PERCENT SUPPORTED</u>
-------------	--------------------------

**FTE Equivalent:**

**Total Number:**

**Sub Contractors (DD882)**

**Inventions (DD882)**

**Scientific Progress**

See attachment.

**Technology Transfer**

# **Final Report**

**(Dates covered: September 01, 2011 to August 31, 2014)**

**Title: Thermal Properties of Whispering Gallery Mode Resonators**

- **Program Manager:**

**Dr. William W. Clark (william.w.clark9.civ@mail.mil)**

- **ARO Proposal Number: 60386-EL**
- **ARO Grant Number: W911NF-11-1-0423**
- **PI: Dr. Lan Yang, Profession, Electrical and System Engineering Department, Washington University, St. Louis, MO 63130**

## 1. Introduction

Nowadays IR detectors have many crucial military and civilian applications, ranging from non-contact thermometry and industrial process monitoring, to missile guidance and threat detection<sup>1-4</sup>. IR detectors enable us to see objects through darkness, smoke or fog. There are two categories of IR detectors based on quantum and thermal effects. Quantum IR detectors rely on electron excitations in semiconductors upon absorption of incident IR photons. However, they often require cooling to reduce thermally induced noises associated with the system. On the other hand, thermal detectors such as micro-bolometers rely on detecting the temperature increase as a result of heat generated upon IR radiation and don't require cooling, which can potentially reduce the cost of IR sensor and improve detection sensitivity at room temperature.

In this report we investigate and characterize the sensing performance of ultra-high-quality photonic resonators<sup>5</sup> in response to IR radiation. We use microtoroids<sup>5</sup> as the sensing platform because the toroidal microresonator is fabricated on chip and has a large suspended disk structure which is ideal for receiving IR radiation and allows thermal isolation from the substrate. Microtoroids have very high quality factors (Q factors) in the range of  $10^7$  to  $10^8$  because of their unique fabrication process which involves melting and reflowing glass material that produces extremely smooth surfaces. They also have very small optical mode volume thanks to their micrometer scale sizes. These properties make them extremely sensitive sensors to perturbations that affect resonance conditions, such as changes of temperature and refractive index, nanoparticle/protein bindings, etc. Upon IR incidence, the resonator absorbs the radiation and generates heat. The good thermal isolation between the resonator and substrate boosts the temperature increase in the resonator. This small increase of temperature in turn changes the refractive index of the resonator material and causes shift of resonance frequency. Because of the ultra-high Q factors of microtoroid, even small amount of resonance shift due to slight changes in the refractive index resulting from temperature variation induced by IR radiation can be detected.

To evaluate the thermal characteristics of microtoroid and its performance as IR detectors, we first modeled and measured the thermal conductance and thermal relaxation time constant of microtoroids, and then conducted experiments to study the sensitivity and frequency response of the microtoroids to IR radiation. The experiments involve instruments such as lasers and photodetectors for probing the resonance mode of microcavities, blackbody source and CO<sub>2</sub> laser as IR radiation source, optical chopper for modulation of IR source, oscilloscope and RF spectrum analyzer to measure the electrical signal, Pyroelectric energy sensors and thermal detectors for calibrating IR radiation, and Oxygen plasma etching machine for cleaning and preparing microtoroids. Figure 1 shows the simplified schematics of the typical experimental

setup for characterizing the microtoroid IR detector. IR radiation from the blackbody source is modulated using an optical chopper with given frequency and then impinges on the microtoroid. The fluctuation of transmitted power from the fiber-microtoroid system carries the information of IR radiation and the transmission spectrum is detected by a RF spectrum analyzer. Thus the IR sensing signal can be read by monitoring the spectral amplitude at the modulated frequency. To enhance the collection efficiency of IR light, an IR lens system can be added before the aperture shown in Fig. 1.

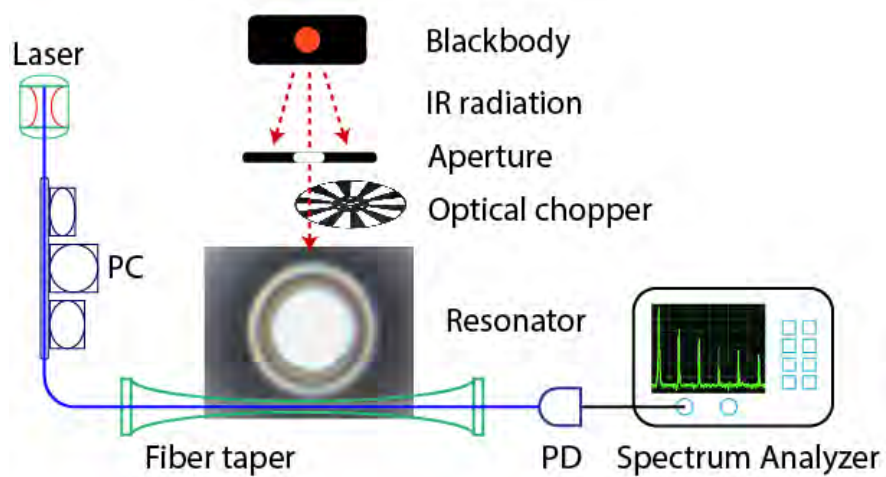


**Figure 1.** Schematic of the setup for characterization of the performance of microtoroid IR detector using blackbody source. Light from a tunable laser is sent through a fiber taper and coupled into the resonator. The distance between the fiber taper and cavity is tunable which changes probe light coupling strength. PC: polarization controller. PD: photo detector.

## 2. Summary of results

### 2.1 Device preparation

We fabricate microtoroids using a four-step process including photolithography, wet etching, Xenon difluoride gas etching and CO<sub>2</sub> laser reflow. We start from 2 micron thick silica on silicon wafers and create arrays of circular disk patterns of photoresist using photolithography, and then the patterned wafer is etched using buffered hydrochloride solution to create circular silica disks. After the photoresist is removed, the wafer is etched using Xenon difluoride gas to undercut silicon beneath the silica disk, which creates a suspended disk structure supported by a silicon pillar. The last step of fabrication is to use a focused CO<sub>2</sub> laser beam to melt and reflow the under-cut silica disk to form a toroidal structure which has an extremely smooth surface that enhances optical quality. Oxygen plasma etching is used during the fabrication process to remove organic materials left on the microtoroid. It is also used to prepare the microtoroid to increase the bonding between the microtoroid and polymer coating that modifies the thermal

response of the resonator. Light from a tunable laser diode is coupled into the microtoroid resonator via a fiber taper (Fig. 2), which was fabricated using the well-established heat and pull method: A single mode fiber is continuously heated on a hydrogen flame while two step motors pull the fiber in different directions until the waist diameter of the taper reached a desired size<sup>6-8</sup>. The same fiber taper was used to couple out the light from the WGM of the resonator. In order to probe the resonances of the microtoroid and the changes in their spectral properties (linewidth and resonance frequency) in response to IR radiation and thermal perturbations, the wavelength of the laser was scanned linearly and the transmission spectra were monitored by a photodetector. High-Q resonance modes were identified and the effect of thermal changes and IR radiation on these resonance modes was measured.

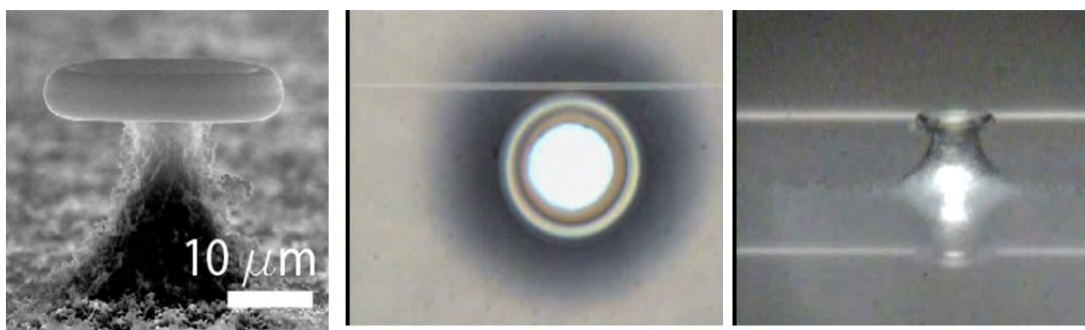


**Figure 2.** Microscope images of typical silica microtoroid resonators used in the experiments. (left) SEM image. (middle) Top view of a microtoroid resonator taken by an optical microscope. (right) Side view of the same microtoroid resonator taken by an optical microscope. The horizontal line close to the resonator is the coupling fiber taper.

Increasing the thermal isolation between the resonator and the substrate can increase the temperature raise upon IR incidence. This can be done by reducing the size of supporting silicon pillar and increasing the microresonator disk area. To achieve a thin pillar and large disk, we fabricated microtoroids with large diameter in the range of 120-160  $\mu\text{m}$ , and then repeated the etching process for the silicon underneath the resonator until we obtained a very thin pillar. Figure 3 shows the reduction of pillar size of the same microtoroid after a few rounds of silicon etching process.



**Figure 3.** Side view images of the same microtoroid showing the reduction of pillar size after several rounds of silicon etching process.

## 2.2 Thermal measurement of microtoroids

The kinetic thermal property of the microtoroid is governed by two parameters: the thermal conductance ( $G$ ) between the microtoroid and environment and the thermal capacity ( $H$ ) of the microtoroid. Without any heat input, the temperature of the resonator will undergo exponential decay to the environmental temperature with a time constant given by  $\tau=H/G$ , which is the thermal relaxation time constant of the resonator. It is a very important parameter as shorter  $\tau$  means larger response bandwidth for the IR sensor. In this project we demonstrated two schemes to experimentally measure the thermal relaxation time constant of microtoroidal resonators. The first method is to use a probe-pump scheme in which the pump laser heats up the resonator. The second scheme is to scan a tunable laser across two nearby optical modes. We experimentally characterized the relation between thermal relaxation time and pillar diameter and major diameter. Moreover, a theoretical model involving material properties and structure parameters was established to estimate thermal relaxation time constant of microtoroids. Finally, finite-element simulations were done to confirm the results.

Due to the ultra-high Q factor of silica microtoroids, even a very small amount of light coupled into the resonance mode leads to very high intracavity powers. Combined with the small mode volume of these resonators, the weak input light leads to a significantly high intensity of light within the cavity. Absorption of this optical field by the silica results in an increase in temperature, which subsequently changes the effective refractive index of the resonator through thermo-optic effect leading to a shift in the resonance frequency<sup>9</sup>.

We developed a pump-and-probe thermal scanning scheme<sup>10</sup> to measure the thermal relaxation time of the microtoroid resonators. In this scheme we used two tunable lasers. One of the lasers served as the probe; it was kept at such low powers and coupled to a low-Q mode that it did not lead to any thermal effect. It was used to monitor the thermally induced changes in the resonance. The other laser was set as the pump with high power and was on resonance with a high-Q mode to induce thermal effects. Conventionally, a resonance spectrum is acquired while the wavelength of a probe laser is scanned linearly across the resonance. Our thermal scanning scheme employs a technique that is just the opposite, i.e., we fix the wavelength of the probe laser and scan the cavity resonance wavelength linearly across the probe laser by tuning the temperature of the cavity.

During linear up-scanning of the pump wavelength, a triangular waveform in the transmission spectrum is obtained<sup>11</sup>. Previous experimental and theoretical studies<sup>10, 11</sup> reveal that the cavity resonance wavelength closely follows the wavelength of the pump during the linear regime of the triangular waveform, and that the cavity temperature also linearly increases (Fig. 4). This can be understood by the proportionality between resonance shift and temperature change.

During this thermal linear up-scanning of the resonance wavelength, the probe cavity resonance changes linearly.

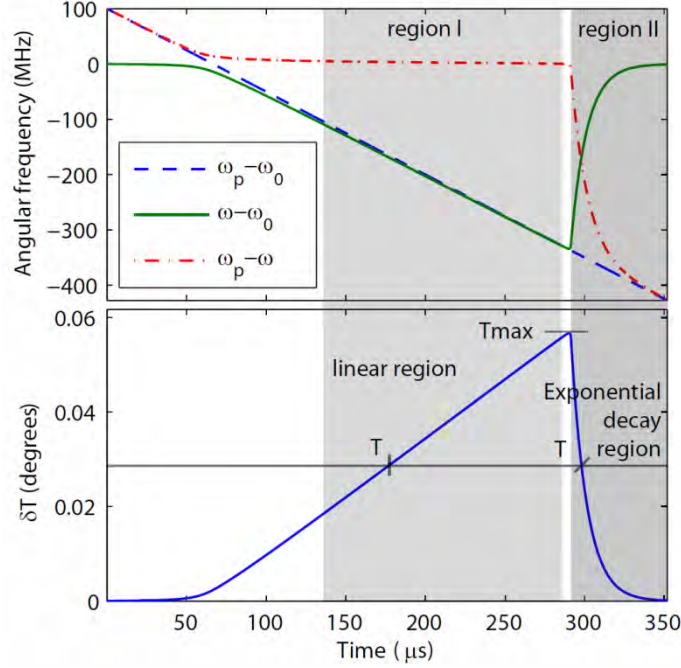


**Figure 4.** The upper panel shows the calculated frequency of scanning pump resonance ( $\omega_p$ ) and cavity resonance ( $\omega$ ) relative to the initial resonance frequency ( $\omega_0$ ), and pump-cavity detuning ( $\omega_p-\omega$ ). The calculation is done under very weak under-coupling condition to clearly manifest region II. The lower panel shows the calculated temperature change of the WGM.

Thermal relaxation time constant ( $\tau$ ) of a microtoroid can be directly measured using this scheme. The probe resonance position gives a constant temperature reference  $T$  (Fig. 4). When the cavity temperature passes  $T_{\max}$  (see Fig. 4), it undergoes exponentially decays and comes across  $T$  again, which generates another resonance dip (Fig. 5(a)). The time period  $t$  between  $T_{\max}$  and the second  $T$  should satisfy  $T/T_{\max} = e^{-t/\tau}$ . Since  $T/T_{\max} = t_1/t_2$  (Fig. 4 and Fig. 5), in experiments, the values of  $t_1, t_2, t$  are acquired from the transmission spectra (Fig. 5(a)). Measured data of  $t$  versus  $t_1/t_2$  are given in Fig. 5(b) for two microtoroids. Coupling condition is varied in this measurement to generate different  $t_1, t_2, t$  values. Exponential fitting to the data gives the thermal time constants. As expected, for microtoroids of similar sizes, larger pillar provides a better heat conductance between the silica toroid and the substrate, and as a result the thermal time constant is smaller.

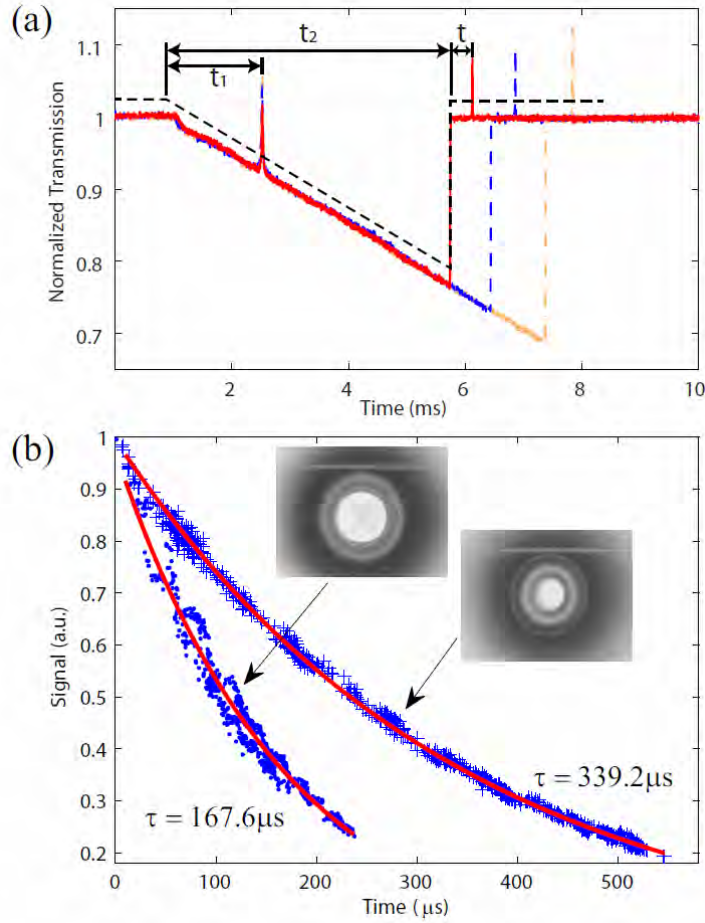


**Figure 5.** (a) Normalized pump transmission (triangles) subtracted by the probe transmission (peaks). The red (solid), blue (dashed) and green (dash-dotted) curves represent the spectra at different coupling conditions. The black dashed line is a fitting to the triangle in the red curve. It is up-shifted for a clear view. (b) Thermal relaxation time constant measurements for the two microtoroids shown in the insets. Red lines are fitting curves.

In addition to the first pump-and-probe scheme, we also developed another new scheme which is simple yet elegant to accomplish the thermal relaxation measurements using only one tunable laser. The setup we used in this experiment is given in Fig. 6.

The principle of our method is shown in Fig. 7. Two nearby resonance modes with high quality factor in a microtoroid are found. A pump laser is linearly scanned to generate the transmission spectrum. Initially, the resonator is operated in under-coupled condition, which yields two tiny resonance dips in the transmission spectrum (Fig. 7a). The time between the two resonance modes are recorded to quantify the distance between these two modes. Then we increase the coupling strength, and as a result of the heating from the laser and opto-thermal effect<sup>9, 10</sup>, the resonance appears as a semi-triangle in the transmission spectrum (Fig. 7c). During the linear scan regime, the resonance wavelength of the cavity closely follows the pump laser wavelength,

and the temperature within the cavity increases linearly. After the pump wavelength pass the resonance of the first mode, the cavity cool down quickly and the pump laser goes out of resonance immediately, which results in a sharp edge in the transmission spectrum. The temperature of cavity experiences exponential decay according to time constant  $\tau$  until the

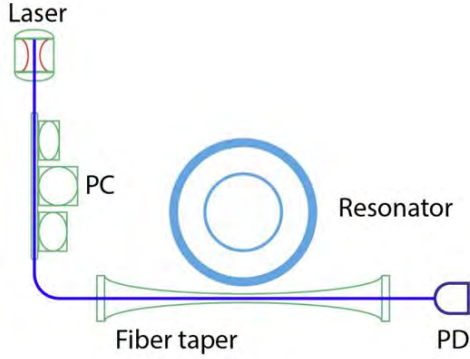


**Figure 6.** A simplified scheme used for characterizing the thermal relaxation time of silica microtoroid resonators. Light from a tunable laser is sent through a fiber taper and coupled into the resonator. The distance between the fiber taper and cavity is tunable which changes coupling strength. Increasing coupling strength by decreasing the taper-resonator distance increases the optical power inside the cavity and hence the temperature of the resonator. PC: polarization controller. PD: photo detector.

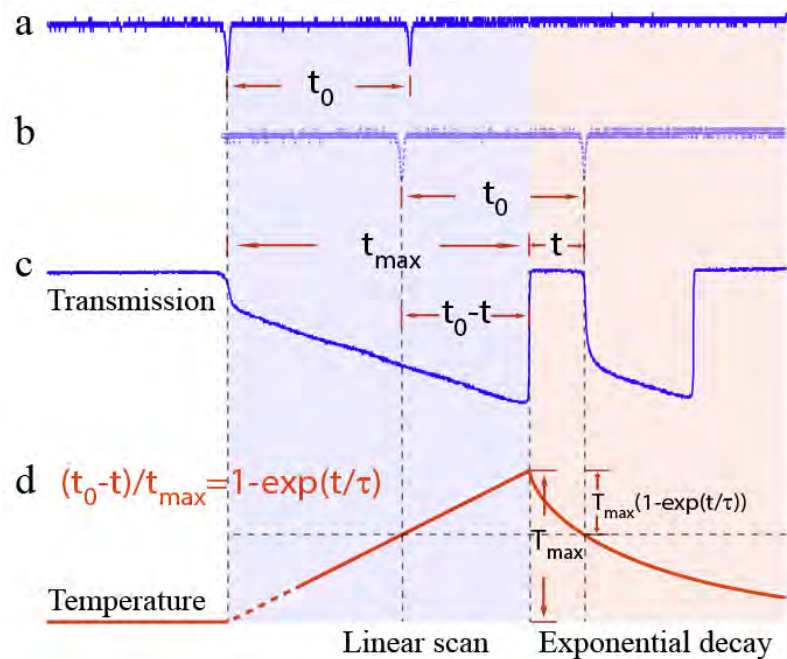
pump laser is on resonance with the second mode. If the second mode is close to the first one, the cavity does not have enough time to decay back to its original temperature before the second mode appears in the transmission spectrum. Then the second mode will be closer to the first mode in the transmission spectrum due to higher cavity temperature, and the distance between them is defined as  $t$  as shown in Fig. 7c. Using Fig. 7b-7d, we find relation

$$\frac{t_0 - t}{t_{max}} = 1 - e^{-t/\tau}$$

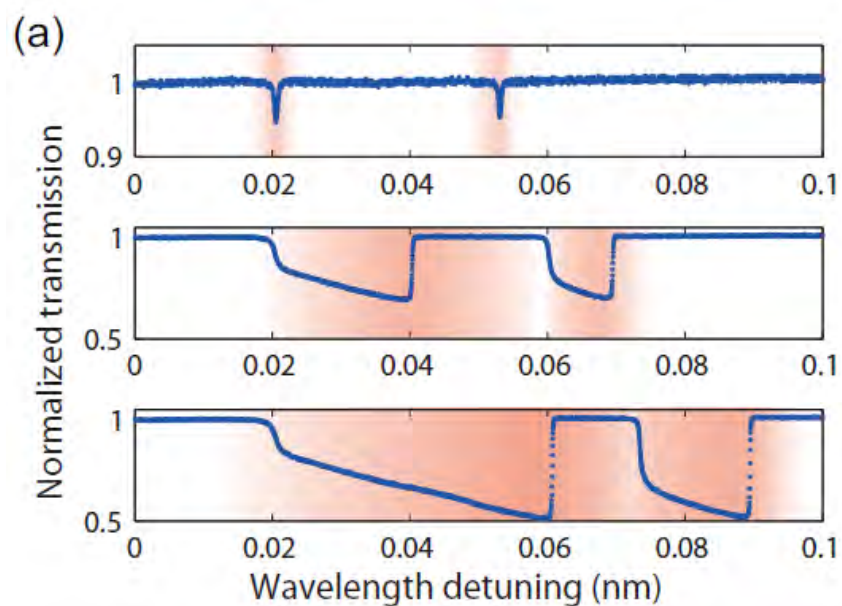
Then using the transmission spectra obtained at different coupling conditions which determine the value of  $t$  and  $t_{max}$ ,  $\tau$  can be estimated.

As shown in Fig. 8a, the fiber taper-microtoroid coupling system can be tuned from under- to over-coupling to generate different  $t$  and  $t_{max}$  values. In the experiments, we continuously change the distance between the fiber taper and the microtoroid, and record the transmission spectra. The relation between normalized temperature response ( $(t_{max} - t_0 + t)/t_{max}$ ) and  $t$  is plotted in Fig. 8b and the results are fitted by exponential decay function. Figure 8b shows fitting results of two microtoroids with different pillar sizes. The blue crosses come from transmission spectrum at different coupling conditions, and red curve shows exponential fitting result. Microtoroids with different pillar sizes yield very different thermal decay rate. Larger

pillar size allows better thermal conduction between the microtoroid and substrate thus  $\tau$  is shorter, while thinner pillar leads to longer  $\tau$ .



**Figure 7.** A scheme to measure thermal relaxation time constant ( $\tau$ ) of a microtoroid. **a., c.** show the transmission spectrum of two nearby modes at under- and over-coupling conditions, respectively. **b.** shows the red-shifted positions of these two modes when pump laser begins to overlap with the second mode. **d.** shows the temperature change in microtoroid during pump laser scanning.



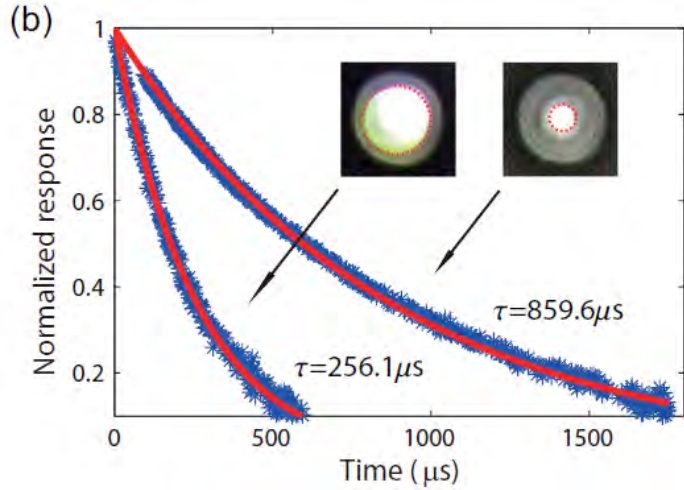


**Figure 8.** Experimental data for the measurement of thermal relaxation time constant ( $\tau$ ) of microtoroids. **a.** Transmission spectra at different air gap conditions, i.e., coupling conditions, for fiber taper - microtoroid system, showing two nearby resonance modes. From top to bottom: air gap decreases. Color is used to show the change of temperature, and red color means higher temperature. **b.** Measurement of thermal relaxation time constant of two microtoroids with different pillar sizes. Blue crosses are experimental data showing the temperature decay, and red curves are theoretical fitting lines. The inset shows the microscopic images of the corresponding microtoroids. Pillars are marked by red dotted circles on the microscopic images. Smaller pillar size leads to longer  $\tau$ .

Geometrical parameters including major diameter, minor diameter and pillar size of microtoroid determine thermal conductance of microtoroid. To systematically study the effect of pillar size on thermal relaxation time, we tested with a single microtoroid and repeatedly reduced its pillar size by  $XeF_2$  gas etching. As seen in Fig. 9a, the thermal relaxation time constant increased from  $200\ \mu s$  to  $1700\ \mu s$  when the pillar diameter was reduced from  $40\ \mu m$  to  $2\ \mu m$ . To examine reliability of this method, for each pillar size, thermal relaxation time was measured 10 times, and the standard deviations of measurements are shown by error bars in the graph. The standard deviation ranges from  $20\ \mu s$  to  $40\ \mu s$ .

The effect of major diameter on thermal relaxation time constant was also studied. Ideally, minor diameter and pillar size of microtoroids should be kept as constants, and only major diameter is changed. However, due to several factors such as  $CO_2$  laser reflow and  $XeF_2$  dry etch in the fabrication process of microtoroids, it is difficult to realize the ideal case. Here, we fabricated four microtoroids with minor diameters of  $7.2 \pm 1.4\ \mu m$ , the pillar diameters in the range of  $15 \pm 0.5\ \mu m$ , and major diameters from  $50\ \mu m$  to  $110\ \mu m$ . As shown in Fig. 9b, the thermal relaxation time increased from  $300\ \mu s$  to  $1300\ \mu s$  when the major diameter increased from  $50\ \mu m$  to  $110\ \mu m$ . Microtoroid with larger major diameter or smaller pillar size has larger

distance between microtoroid ring and pillar, which reduces thermal conductance between the mode volume and the substrate, as a result, the thermal relaxation time is longer.

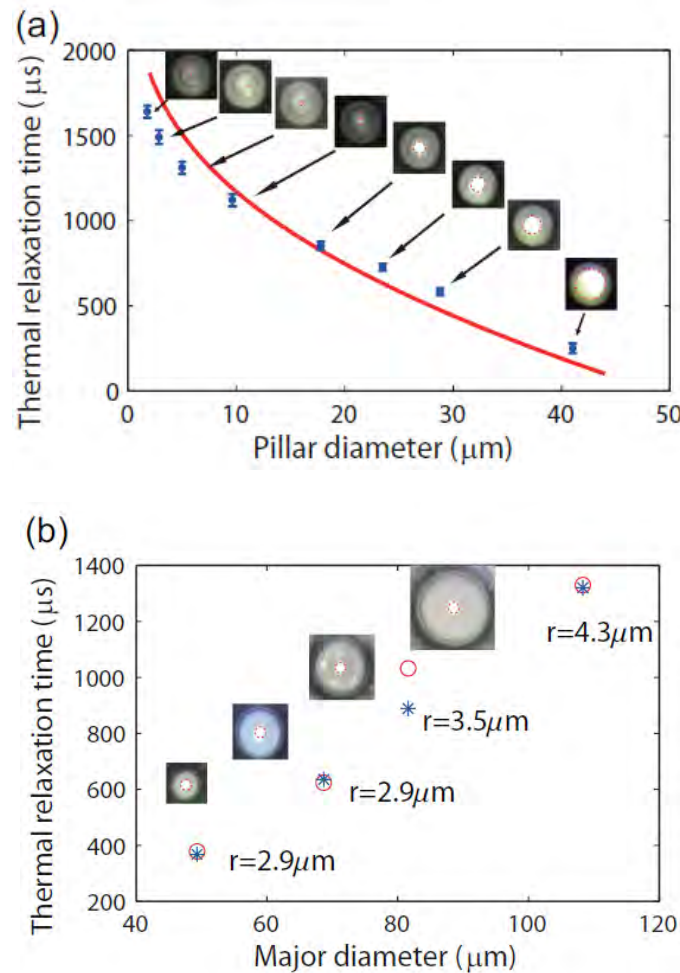


**Figure 9. a.** Measured thermal relaxation time constant ( $\tau$ ) for the same microtoroid with different pillar sizes. The microtoroid has a major diameter of 64  $\mu\text{m}$  and was repeatedly etched to reduce its pillar diameter down to 2  $\mu\text{m}$ . For each pillar diameter, thermal relaxation time was measured 10 times to obtain the standard deviation of measurements as shown by error bars in the graph. Blue crosses are experimental data, and red curve is from analytical expression based on our model. **b.** Thermal relaxation time constants for microtoroids with different major diameters. The minor diameters are in the range of  $7.2\pm1.4\ \mu\text{m}$ , and the pillar diameters are in the range of  $15\pm0.5\ \mu\text{m}$ . Blue crosses are experimental data, and red circles are from analytical results based on our model. The inset pictures show the microscopic images of the corresponding microtoroids. Pillars are marked by red dotted circles in the microscope images.

To better optimizing microtoroids for IR sensing, we build a analytical model to estimate the thermal relaxation time taking into consideration both material properties and microtoroid geometries. Figure 10 shows the side view and top view of a microtoroid. The geometric

parameters of microtoroid including major radius  $R$ , minor radius  $r$ , and pillar radius  $p$  are labeled in the figure. The thickness of the disk  $d$  is assumed to be a known parameter, and measured to be  $2 \mu\text{m}$  in our microtoroids. Thermal properties of materials including density  $\rho$ , thermal conductivity  $\lambda$ , and capacity  $c$  are considered in this model.

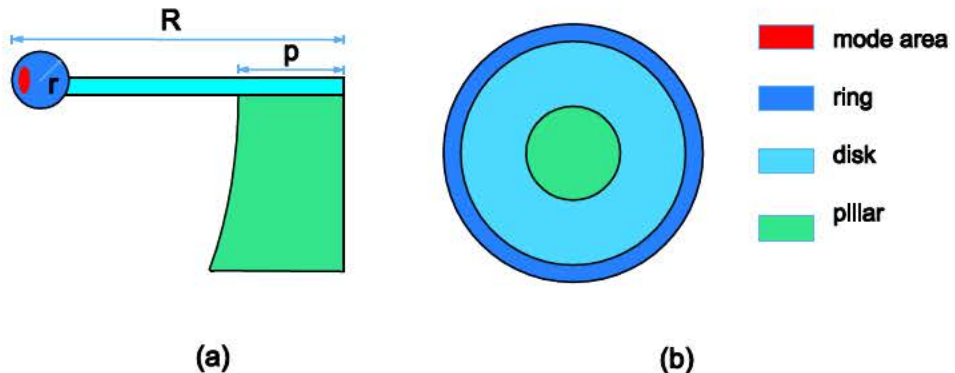


**Figure 10.** Structure of a microtoroid consisting of three parts: ring, disk and pillar. Different colors are used to distinguish different parts in the figure. a. Side view. b. Top view.

This model is based on three approximations of heat transfer process in the microtoroid. First, the time that heat transfers from mode volume to the ring is much smaller than the time of heat transfer from the ring to the substrate, which is confirmed by the Comsol simulation. Thus, we consider the ring has the same temperature  $T_1$ . Second, due to much larger thermal conductivity of silicon than silica, we treat the silica area on top of pillar as part of the pillar, and neglect the time that heat transfers from pillar to substrate, i.e. the whole pillar is always at room temperature  $T_2$ . Third, the effect of air is neglected (later an empirical correction term is added to the model to include the effect of air).

In this model, toroid is divided into three parts: ring part with same temperature  $T_1$ , pillar part with a constant temperature  $T_2$ , and disk part which serves as a round heat transfer tube. Thus the thermal relaxation time is determined mainly by the thermal capacity of ring and heat transfer coefficient of disk. Intuitively, larger capacity of ring or smaller conductance of disk will give longer thermal relaxation time.

To further simplify the analysis, we also make several approximations for the microtoroid structures. For the ring, we treat it as a standard torus with major radius  $R$  and minor radius  $r$ , neglecting its slight deformation and nonuniformity as seen in experiments. Thus, the mass of the ring  $m$  can be expressed as:

$$m = 2\pi^2(R-r)r^2\rho,$$

where  $\rho$  is the density of silica. For the disk, we treat it as a circular tube with thickness  $R-2r-p$ , and length of  $2 \mu\text{m}$ . Such a structure has thermal conductance  $k$  determined by following expression:

$$k_0 = \frac{\lambda}{R-2r} \frac{1}{\ln(\frac{R-2r}{p})},$$

where  $\lambda$  is the thermal conductivity of silica. The contact area  $A$  between ring and disk is chosen to be lateral area of disk, expressed as

$$A = 2\pi(R-2r)d$$

From heat transfer theory, we have

$$mc \frac{dT_1}{dt} = k_0 A (T_2 - T_1),$$

and solution to this differential equation is

$$T_1 = e^{-\frac{k_0 A}{mc} t} + T_2$$

By definition, thermal time constant  $\tau$  is determined by

$$\tau = \frac{mc}{k_0 A} = \frac{\pi \rho c}{\lambda d} (R-r)r^2 \ln(\frac{R-2r}{p})$$

When pillar size is large, we assume that the effect of air is negligible because most of heat is transferred from mode volume to the substrate through pillar. However, when pillar size becomes very small, the amount of heat dissipating through pillar is comparable to that transfers through air. Then the effect of air cannot be neglected anymore. Thus we need to add a correction term to the expression above to consider the effect of air.

Here we define  $k_1 = \alpha(R^2 - p^2)$  as the correction term of heat conductance, where  $\alpha$ , with dimension  $\text{W} / \text{m}^4 \cdot \text{K}$ , is regarded as a constant related to the thermal properties of air. Thus overall thermal conductance  $k$  becomes:

$$k = k_0 + k_1$$

and the revised thermal relaxation time constant  $\tau$  is:

$$\tau = \frac{mc}{kA} = \tau_0 \frac{1}{1 + \frac{k_1}{k_0}} = \frac{\pi \rho c}{\lambda d} (R-r)r^2 \ln(\frac{R-2r}{p}) \frac{1}{1 + \frac{\alpha}{\lambda} (R^2 - p^2)(R-2r) \ln(\frac{R-2r}{p})}$$

To determine the parameters in the above formula, we measured thermal relaxation time of 30 microtoroids with different major diameters, minor diameters and pillar sizes. Then we use these experiment data to examine the analytical expression above.

We can get information for the parameters of microtoroid geometry and material properties in the analytical expression from measurement and literatures. However, the values we obtain may not match with the real case. The size of microtoroid is measured under optical microscope. Minor diameter, which is very small compared with major diameter and pillar size, is difficult to measure precisely in this way. Therefore we consider a systematic correction term for the minor diameter and use it as a fitting variable in the analytical expression. The parameters of material properties including density, thermal conductivity, and thermal capacity are obtained directly from literatures and they may differ slightly from the real values. Also, the nominal thickness of disk is 2  $\mu\text{m}$  as claimed by the wafer manufacturer but could be slightly different. All these errors will lead to mismatch between analytical result and experiment data. Thus we add a correction constant  $\beta$  for the system to compensate these factors. Air correction coefficient  $\alpha$  is another free fitting parameter. The information for major diameter and pillar size of the microtoroids is obtained from experimental measurements.

Thermal conductivity $\lambda$	1.4 W/m•K
Thermal capacity $c$	700 J/K•Kg
Density $\rho$	2200Kg/m <sup>3</sup>
Thickness of disk $d$	2 $\mu\text{m}$

**Table 1.** Parameters used in the model of thermal relaxation time constant

Minor radius $r$	1.3 $r$
$\alpha$	$1.29 \times 10^{-11}$ W/m <sup>4</sup> •K
$\beta$	1.3780

**Table 2.** Values of fitting parameters in the model of thermal relaxation time constant

Values of parameters used in the fitting program are displayed in Table 1. To determine the free fitting parameters  $r$ ,  $\alpha$  and  $\beta$  in the expression for  $\tau$ , we use least square root fit for the normalized error of all data. The fitting results can be seen in Table 2. From the results, we get the average fitting error of 16.3%, which shows that this simple model works well. Figure 11 shows effect of pillar diameter on the thermal relaxation time, and Fig. 12 shows the relation between thermal relaxation time and the ratio of pillar size to major diameter. As expected from the analytical expression, larger ratio of pillar size to major diameter will yield a shorter thermal relaxation time. Based on the model and parameters obtained, we compare the theoretical thermal relaxation time to experimental data for different pillar sizes at fixed major and minor diameter (Fig. 13), and different major diameters at fixed minor and pillar size (Fig. 14).

With the analytical model of thermal relaxation constant, we can conveniently quantify the effective thermal conductance and capacitance of a microtoroid given its geometric parameters. Therefore we can better predict the performance of a microtoroid IR sensor.

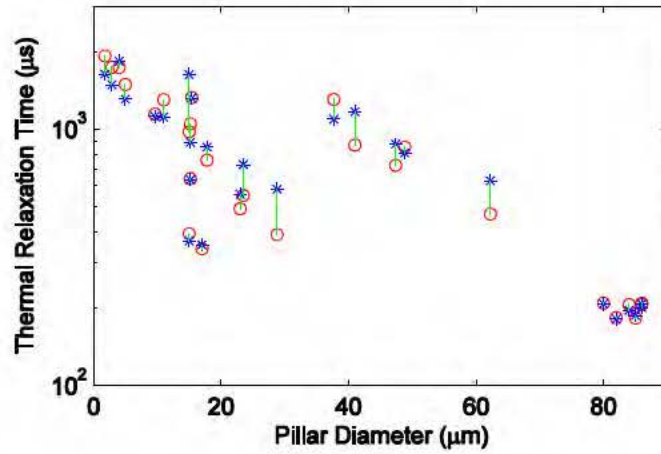


**Figure 11.** Thermal relaxation time constant  $\tau$  for microtoroids with different pillar sizes. Blue stars show the experiment data, and red circles show the corresponding calculated results. Green bars linking experiment data with corresponding analytical results designate the difference.

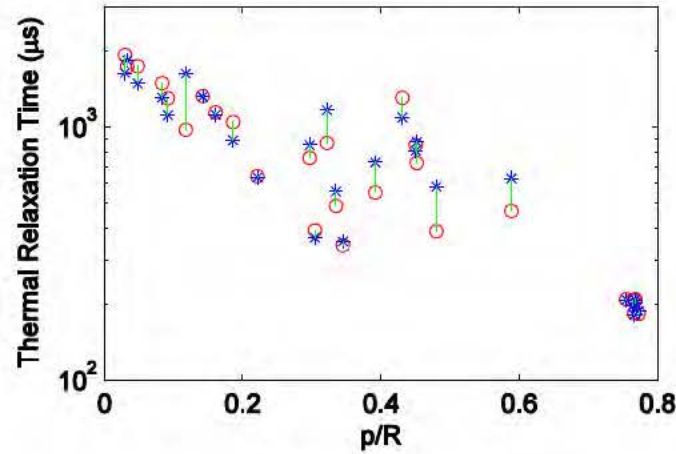


**Figure 12.** Thermal relaxation time constant  $\tau$  for microtoroids with different ratios of pillar diameter to major diameter. Blue stars show the experiment data, and red circles show the analytical results. Green bars linking experiment data with corresponding analytical results designate the difference.

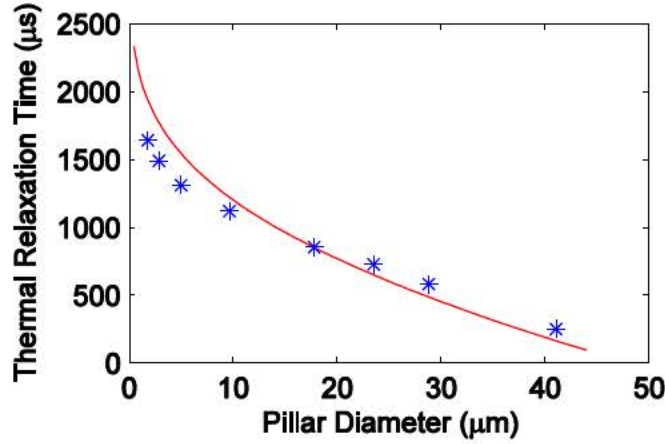


**Figure 13.** Thermal relaxation time constant  $\tau$  for microtoroids with different pillar sizes. The blue stars are experiment data, and the red line is calculated from the analytical expression.

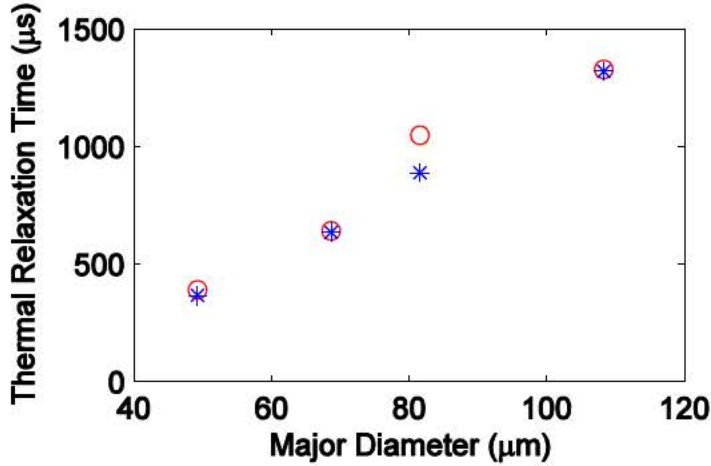


**Figure 14.** Thermal relaxation time constant  $\tau$  for microtoroids with different major diameters. The blue stars are experiment data, and the red circles are corresponding analytic results.

Moreover, we developed a finite element simulation (FEM) to confirm the thermal transport model presented above. The structure of microtoroid is the same with previous analytical model consisting of ring, disk, and pillar. A silicon substrate is added in the model serving as a heat sink to improve the simulation accuracy. The core area inside the ring (i.e. the optical mode) is set to an initial temperature 320K, and the rest parts of the microtoroid and surrounding air are set to 300K. The temperature of bottom surface of substrate is fixed at 300K. The temperature evolution over the whole system is monitored. Figure 15 shows the temperature distribution at four different times. In Fig. 15(b,c), the temperature in surrounding air is much larger than the temperature in the center area of the disk. The reason is that the heat capacity of air is extremely small compared with silica, and even a small amount of heat

from microtoroid ring could induce a large temperature increase. Figure 16 shows the heat flux distribution at four different times, from which we could see that most of heat energy in the mode area is transported through the disk to the pillar. Thermal relaxation time could be obtained by fitting the temperature evolution in the mode area using exponential function. One example is shown in Fig. 17, with thermal relaxation time of 914  $\mu$ s.

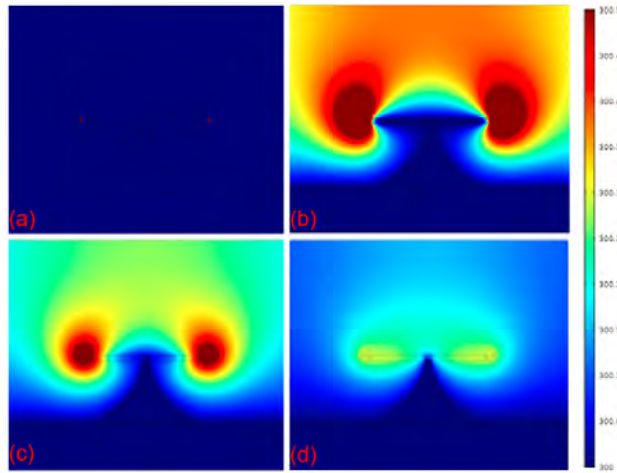


**Figure 15.** Temperature distribution in the cross section of the microtoroid at four different times (a)  $t=0 \mu\text{s}$ , (b)  $t=2 \mu\text{s}$ , (c)  $t=50 \mu\text{s}$ , (d)  $t=500 \mu\text{s}$ . The temperature values are described by color bar. The core of the microtoroid is set to 320K and the rest of the system is 300K at  $t=0\mu\text{s}$ . Major and minor diameter of the microtoroid is 60 and 5  $\mu\text{m}$  respectively, and the disk thickness is 2  $\mu\text{m}$ .

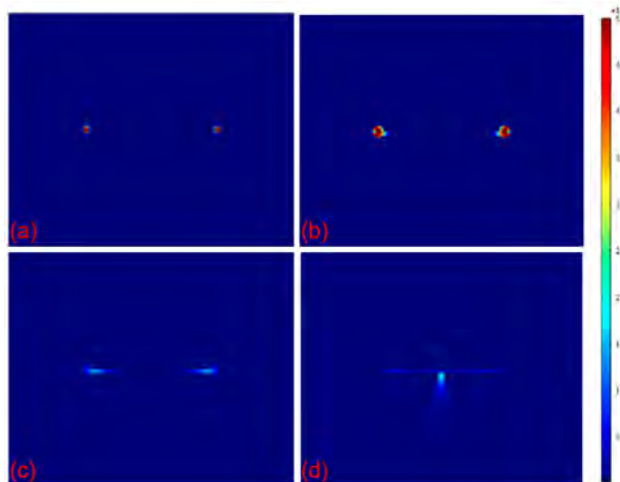


**Figure 16.** Heat flux distribution over cross-section of the microtoroid at four different times (a)  $t=0 \mu\text{s}$ , (b)  $t=2 \mu\text{s}$ , (c)  $t=20 \mu\text{s}$ , (d)  $t=100 \mu\text{s}$ . The heat flux values are described by color bar. The core of the microtoroid is set to 320K and the rest of the system is 300K at  $t=0\mu\text{s}$ . Major and minor diameter of the microtoroid is 60  $\mu\text{m}$  and 5  $\mu\text{m}$  respectively, and the disk thickness is 2  $\mu\text{m}$ .

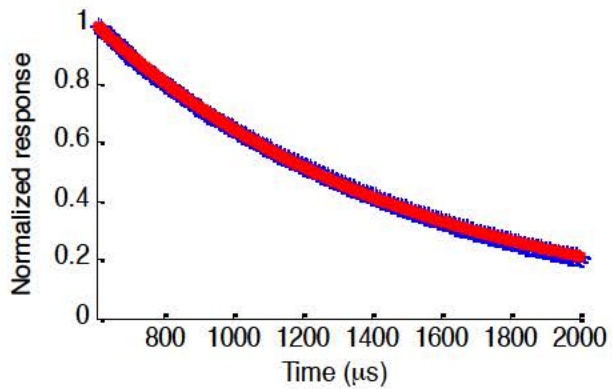


**Figure 17.** Analysis of thermal relaxation time of the microtoroid. Blue stars are data obtained from FEM simulation, and red curve is the theoretical fitting line.

The effects of geometrical parameters including pillar diameter, major diameter, and minor diameter on thermal relaxation time are investigated by this FEM model. When investigating the effect of pillar diameter, the other two parameters (i.e. major diameter, minor diameter) are fixed. At each pillar size, the temperature evolution at mode area is monitored and fitted to get the thermal relaxation time. Then we obtain relation between thermal relaxation time and pillar size. The same method is used to investigate effects of major diameter and minor diameter. The results are shown in Figs. 18-20, which show the same trend with experimental and analytical results.

The thermal relaxation time given by FEM simulation has a noticeable difference from the experiment result. The reasons come from two parts. First, the FEM model only considers the effect of air conduction, while in the real case the air convection may play a more important role. And the structure of microtoroid in the model is slightly different from that in real case such as geometry of ring, pillar shape. All these factors can lead systematic errors between experiment data and FEM simulation results. Second, the parameters used in the FEM model may not be the same as those in the real case. The geometrical parameters including major diameter, minor diameter, pillar size are obtained under an optical microscope, which leads to measurement error. The parameters of material properties including density, thermal conductivity, and thermal capacity are obtained from literatures, thus it is possible that these parameters do not match with real parameters in our device. Also, the thickness of disk may not be exactly 2  $\mu\text{m}$  as the manufacture claims. All these parameter errors will lead to mismatch between the experiment data and the FEM simulation results. However, the trends revealed in simulations are the same as those observed in experiments.

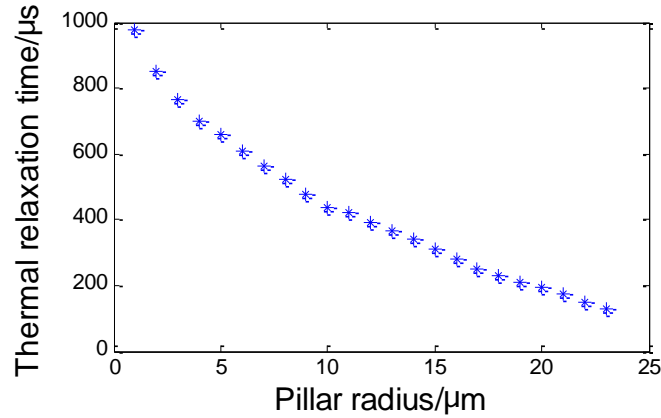


**Figure 18.** Thermal relaxation time for microtoroids with different pillar radius  $p$ . The major radius  $R$  and minor radius  $r$  are fixed at  $R = 29.5 \mu\text{m}$ ,  $r = 2.5 \mu\text{m}$ .

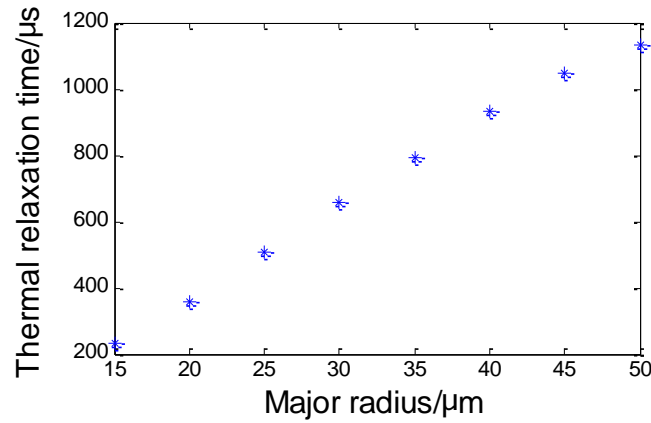


**Figure 19.** Thermal relaxation time for microtoroids with different major radius  $R$ . The pillar radius  $p$  and minor radius  $r$  are fixed at  $p = 5 \mu\text{m}$ ,  $r = 3 \mu\text{m}$ .

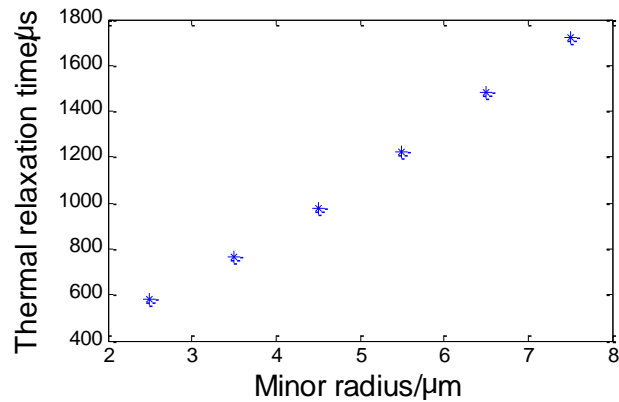


**Figure 20.** Thermal relaxation time for microtoroids with different minor radius  $r$ . The major radius  $R$  and pillar radius  $p$  are fixed at  $R = 30 \mu\text{m}$ ,  $p = 5 \mu\text{m}$ .

In short, we have demonstrated the methods to experimentally measure thermal conductance and thermal relaxation time of microtoroid. The relation between geometrical parameters of microtoroid and thermal relaxation time is investigated both experimentally and theoretically. This study helps better understand thermal properties and effect in microresonators. Moreover, the knowledge is useful to optimize the geometry of microtoroid for IR sensing application. This method can also be applied to characterize thermal property of other types of whispering gallery mode resonators.

### 2.3 Characterization of IR detectors based on microtoroid resonators

In this section, we characterize the performance of a silica microtoroid resonator for detecting IR radiation. The underlying principle of IR detection is as follows. The incident IR radiation absorbed by silica microresonator increases the resonator temperature. As a result the thermo-optic effect<sup>9, 10</sup> kicks in and leads to a change in the refractive index, which in turn shifts the resonance wavelength. The higher the incident IR radiation is, the larger the shift in the resonance wavelength is. The resonance shift can be detected either by scanning the wavelength of a probe light from a tunable laser around a WGM resonance and recording the change in the resonance after each scanning or by locking the wavelength of the probe on the resonance slope and monitoring the intensity fluctuations of the transmitted light.

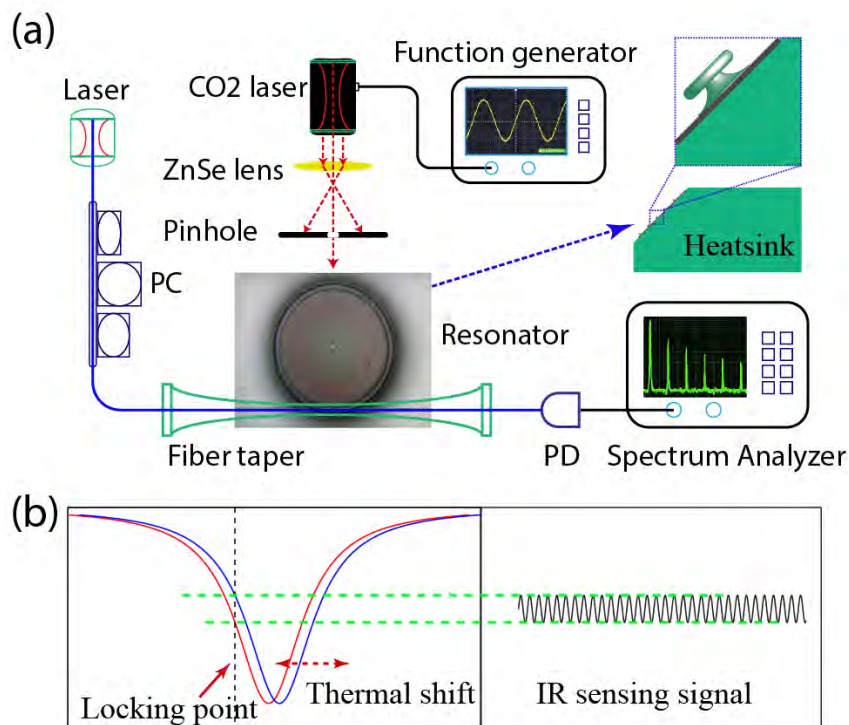


**Figure 20.** Experimental scheme for characterizing the performance of microtoroid IR sensor using a CO<sub>2</sub> laser. **a.** Simplified experimental setup. The inset shows image of the microtoroid used in our experiments together with the fiber taper used to couple the probe light in and out of the resonator. **b.**

Illustration of the IR detection scheme. When the probe laser is locked on the resonance slope, the output signal fluctuates at the modulation frequency of the incoming IR light. The microtoroid has major diameter of around 100  $\mu\text{m}$  and its pillar is etched to very small size ( $<2 \mu\text{m}$ )<sup>9</sup>.

The experimental setup used to characterize the performance of our IR detector is shown in Fig. 20. We used a pulse-width modulated CO<sub>2</sub> laser with a wavelength of 10  $\mu\text{m}$  and a maximum output power of 30 W as the IR source to conduct this study, because silica has a strong absorption at 10  $\mu\text{m}$  wavelength. The beam from the CO<sub>2</sub> laser was first expanded by a ZnSe lens and then passed through a small pinhole with a diameter of 381  $\mu\text{m}$  to control the illumination area on the microtoroid, and to block the light incident on the surrounding area of the resonator. Only a small fraction of total IR radiation passes through the pinhole and reaches at the resonator. The microtoroid was placed at an angle of 45 degrees on a heat sink to allow optical imaging and to stabilize its base temperature. We used a probe light from a tunable external cavity laser in the 1450 nm band to monitor the effect of the IR radiation on the transmission spectra and the resonance frequency of the microtoroid. The CO<sub>2</sub> laser was modulated with an external gating source with a known frequency. As a result, when the probe laser was locked on a resonance slope (Fig. 20b), the transmission contained the frequency component of modulation, which allowed an easy detection with high signal-noise-ratio using a spectrum analyzer.

The microtoroid used in the experiments had a major diameter of about 100  $\mu\text{m}$ , and its pillar was etched to have a size less than 2  $\mu\text{m}$  to maximize thermal isolation from the silicon wafer which acts as a thermal sink. The fiber taper that was used to couple the probe light in and out of the WGM was in contact with the microtoroid to stabilize the coupling condition and reduce vibration of the fiber taper. In this situation, we measured the loaded Q factor as  $7.8 \times 10^6$ . Figure 21a shows the transmission spectrum of the system. First, we modulated the IR source at 100 Hz and monitored the transmission of the probe light through fiber-resonator system. Figure 21b shows the frequency spectrum of the measured transmission. Despite the noise components, a prominent peak at 100 Hz is clearly seen above the noise floor, confirming the response of the resonator to IR radiation. The signal-to-noise ratio (SNR) was about 260 in this measurement. The low frequency noise (<200Hz) was mainly from mechanical vibrations of the resonator system and the tunable laser. The narrow distinct peaks (e.g. at 60Hz and 300Hz) are electrical noises. We observed that even the fan noise from instruments was significant enough to disturb the measurement, suggesting that in a real application the resonator-taper system should be well-isolated, probably in a vacuum chamber, to lower the noise floor and increase the SNR.

To study the frequency response of the IR detector, we varied the modulation frequency of the CO<sub>2</sub> laser. The IR detector shows typical features of frequency response of a low pass RC filter.

When the modulation frequency is low, the temperature changes of the microtoroid can keep up with the gated IR radiation and thus the transmission shows square waves with exponentially decaying edges. As the frequency increased, the amplitude of the response decreased and the transmission transformed into semi-triangle waves because of the limited bandwidth set by the thermal relaxation time of the resonator. Next, we investigate the response of the IR detector at different regimes of frequency detuning between the probe laser and the cavity resonance. At low powers, the probe laser doesn't have any significant effect on the thermal characteristics of the IR detection mechanism. Therefore the IR response is the same regardless of whether the probe laser is on the red- or blue- detuned side of the resonance. However, when the power of the probe laser is higher than a few  $\mu\text{W}$ , there is a noticeable heating effect in the resonator due to its high Q and good thermal isolation. As a result increased temperature in the resonator red-shifts the resonance and affects the IR response differently on the blue- and red- detuned slopes of the resonance<sup>9</sup>.

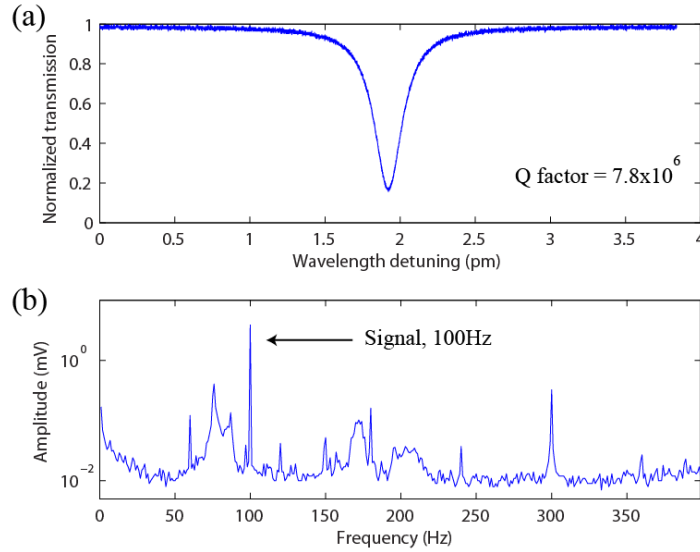


**Figure 21.** (a) Transmission spectrum of the microtoroid resonator used to perform the IR measurements. (b) Frequency spectrum of the transmission of the resonator system when the 1450 nm probe laser was locked on the resonance slope with a blue detuning with respect to a WGM resonance. A clear peak at 100 Hz with SNR of 260 shows the detection of IR radiation. CO<sub>2</sub> laser power was set at 5% of the maximum power.

When the probe laser is on the blue-detuned resonance slope, thermal heating by probe laser increases the device temperature and on-resonance thermal locking effect<sup>9, 10</sup> tries to stabilize the device temperature. Consequently, the detector becomes less sensitive to the thermal heating effect of IR radiation. On the other hand, when the probe laser is on the red-detuned slope, the thermal heating effect by the probe laser keeps the resonator temperature in a slightly unstable regime (opposite to thermal locking effect), which allows higher IR response. In

this case, the IR response is no longer symmetric on both sides of the resonance peak when probe laser power is sufficiently high<sup>9</sup>. To estimate the bandwidth of the microtoroid IR detector, we plot the relation between response amplitude and IR modulation frequency (Fig. 22). The frequency response features a passband and a first order drop-off edge. The frequency response measurement allows us to optimally select the modulation frequency of the incident IR radiation. Ideally one would like to keep the modulation frequency in the passband. We found a good agreement between the measured and theoretically predicted cut-off frequencies. For example, for the black curve in Fig. 22, a cutoff frequency of 80 Hz is calculated from the experimental data, and  $\tau = 1.84$  ms measured for the same microtoroid corresponds to a cutoff frequency of 88.4 Hz.

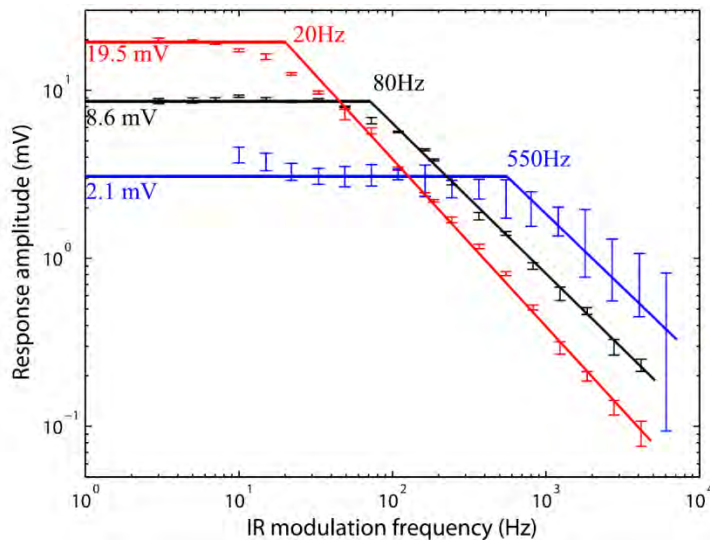


**Figure 22.** Frequency response of the microtoroid IR detector at various power and detuning of the probe laser. Red data points were obtained for low power (about  $6.9 \mu\text{W}$ , or 330 mV measured by the photodetector) and red-detuned probe laser. Black data points (middle) correspond to low power (about  $6.9 \mu\text{W}$ , or 330 mV measured by the photodetector) but blue-detuned probe laser. Blue data points correspond to high power (about  $67.4 \mu\text{W}$ , or 3200 mV measured by the photodetector) and red-detuned probe laser, in which there is a strong heating effect induced by the probe. The CO<sub>2</sub> laser power was set to 5% of its maximum output power, which was about 1.5 W.

Interestingly, we observed that the frequency detuning and the power of the probe laser not only modified the thermal sensitivity of the IR detector but also affected its bandwidth. When a probe laser is blue-detuned from the resonance frequency, it can induce thermal locking effect if it has sufficient power, and increase the detector bandwidth but results in relatively smaller response amplitude. This is because thermal locking tends to keep the system around the locking temperature, which forces the system to return back to this temperature more rapidly when it drifts away. On the other hand, a red-detuned probe laser can increase the response amplitude in the pass-band but with a reduction in bandwidth. This unique feature allows us to

tune the response of the IR detector without modifying its physical structure (Fig. 22). By adjusting the operating power or Q factor of the mode, and detuning of the probe laser, we can tune the sensitivity and bandwidth of the IR detector and optimize its performance at a fixed IR modulation (chopping) frequency.

Finally, we estimated the noise equivalent power (NEP) of our IR detector. Note that the measurements were performed in normal room conditions without actively stabilizing the sensor system or the probe laser. The probe power was set very low that it did not induce significant thermal effect. We obtained the best measurement results when an IR radiation of  $3.58 \mu\text{W}$  (calibrated using a thermopile sensor) was incident on the silica microtoroid. At the modulation frequency of 49 Hz, an SNR of 480 was obtained. This corresponds to an NEP of  $7.46 \text{nW}$ , or IR intensity of  $0.095 \text{ mW/cm}^2$ . This number is mainly limited by the noise floor and can be improved by using a stabilized probe laser and by isolating the sensor system, for example by placing it in a vacuum environment.

In conclusion, we developed an uncooled thermal detector for IR radiation using a silica microtoroid resonator, and evaluated its sensitivity and frequency response. Unique thermal and optical properties of the resonator enable us to tune the sensitivity and frequency response of the IR detector. The sensitivity of the IR detector can be improved by isolating it from external acoustic/mechanical noise sources, as well as by optimizing the resonator structure to allow better thermal isolation from the substrate. For example, one can tailor the disk during fabrication to create a spoke structure (spoke-anchored resonator<sup>12</sup>) to increase the thermal isolation between the resonator and substrate. Moreover, placing the resonator in vacuum environment will eliminate the thermal convection effect and help reduce acoustic/mechanical noise. Due to their ultra-high sensitivity to thermal perturbations and IR radiation as demonstrated here, we believe that microtoroid IR sensors have the potential to compete with the state-of-the-art microbolometer detectors.

## References

1. Rogalski, A. Infrared detectors: status and trends. *Progress in Quantum Electronics* **27**, 59-210 (2003).
2. Rogalski, A., Antoszewski, J. & Faraone, L. Third-generation infrared photodetector arrays. *Journal of Applied Physics* **105** (2009).
3. Talghader, J.J., Gawarikar, A.S. & Shea, R.P. Spectral selectivity in infrared thermal detection. *Light-Science & Applications* **1** (2012).
4. Martyniuk, P. & Rogalski, A. HOT infrared photodetectors. *Opto-Electronics Review* **21**, 239-257 (2013).

5. Armani, D.K., Kippenberg, T.J., Spillane, S.M. & Vahala, K.J. Ultra-high-Q toroid microcavity on a chip. *Nature* **421**, 925-928 (2003).
6. Knight, J.C., Cheung, G., Jacques, F. & Birks, T.A. Phase-matched excitation of whispering-gallery-mode resonances by a fiber taper. *Opt Lett* **22**, 1129-1131 (1997).
7. Little, B.E., Laine, J.P. & Haus, H.A. Analytic theory of coupling from tapered fibers and half-blocks into microsphere resonators. *Journal of Lightwave Technology* **17**, 704-715 (1999).
8. Cai, M., Painter, O. & Vahala, K.J. Observation of critical coupling in a fiber taper to a silica-microsphere whispering-gallery mode system. *Phys Rev Lett* **85**, 74-7 (2000).
9. Zhu, J., Ozdemir, S.K., Yang, L. Infrared light detection using a whispering-gallery-mode optical microcavity. *App. Phy. Lett.* **104**, 171114 (2014).
10. Zhu, J.G., Ozdemir, S.K., He, L.N. & Yang, L. Optothermal spectroscopy of whispering gallery microresonators. *Applied Physics Letters* **99** (2011).
11. Carmon, T., Rokhsari, H., Yang, L., Kippenberg, T.J. & Vahala, K.J. Temporal behavior of radiation-pressure-induced vibrations of an optical microcavity phonon mode. *Physical Review Letters* **94** (2005).
12. Anetsberger, G., Riviere, R., Schliesser, A., Arcizet, O. & Kippenberg, T.J. Ultralow-dissipation optomechanical resonators on a chip. *Nature Photonics* **2**, 627-633 (2008).